Dispersed fringe tracking with the multi-r_o apertures of the Grand Interféromètre à 2 Télescopes

L. Koechlin[1], P. R. Lawson[2], D. Mourard[2], A.Blazit[2], D. Bonneau[2], F.Morand[2], Ph. Stee[2], I.Tallon-Bosc[3], F.Vakili[2]

[1] *Laboratoire Astrophysique de Toulouse, URA 285 du CNRS, 14 avenue E.Belin 31400 Toulouse, France.*

[2] *Observatoire de la Cote d'Azur, Dept. Fresnel, URA 1361 du CNRS, 06460 St. Vallier de Thiey, France.*

[3] *Observatoire de Lyon, 9 avenue Charles André, UMR 142 du CNRS, 69561 St Genis Laval Cedex, France.*

ABSTRACT

A new fringe tracker based on photon counting detectors and real time image processing has been implemented on the "Grand Interféromètre à 2 Télescopes" (GI2T) at the Observatoire de la Côte d'Azur. Fringe visibilities have been recorded on P Cygni and other stars across the Hα emission line with optical path differences stabilized to between 4 and 7 μm rms (1% of the coherence length). This paper presents the first results and describes the principle, implementation and performance of the fringe tracker.

Key Words: astronomy, interferometry, fringe tracking

1 . Introduction

The Grand Interféromètre à 2 Télescopes (GI2T) [1] [2] is a long baseline optical stellar interferometer, located at the Observatoire de Calern, in the Maritime Alps of France. It is notable for its use of large 1.5 meter apertures, broad multi-channel spectral coverage, beam combination in the image plane and photon counting cameras. As such, the instrument is unique among stellar interferometers.

Although the GI2T has been operational since 1985 with the largest apertures among operational interferometers, up until 1994 fringe acquisition and tracking have been performed visually. The fringes are contained in dispersed image slices and appear across speckles, each of which has a limited spatial extent and lifetime. The path-difference is derived from the slope of the dispersed fringes, which are detected even when image slices contain numerous speckles.

In this paper we describe the automated fringe tracker that has been recently commissioned. In Sect. 2 we describe the fringes that are detected in the image plane of the interferometer. In Sect. 3 we present our method of fringe tracking and in Sect. 4 describe its implementation. The performance of the fringe tracker is then discussed and illustrated in Sect. 5.

2 Dispersed fringes

We first describe the fringes ignoring atmospheric turbulence and later generalize our description to include atmospheric effects and the use of multi-r_o apertures, in which case the fringes that form in the image plane appear across individual speckles.

2. 1 Dispersed Fringes in the Image Plane

If atmospheric effects are absent, each aperture produces its own diffraction limited image of the star. As in a Young's double-slit experiment, the superimposed images are modulated by fringes, whose spacing depends on the distance between the remapped pupils. For a given baseline, the intensity in the combined beam can be written,

$$I(\chi, \sigma) = I_s(\sigma)\,[1 + \gamma \cos(2\pi\sigma\chi + \phi)] \tag{1}$$

where χ is the optical path difference, σ is the spectroscopic wavenumber $1/\lambda$, $I_S(\sigma)$ is the stellar spectrum, and γ and ϕ are the modulus and phase of the complex fringe visibility, which for resolved stellar sources may be wavelength dependent. Bright fringes are detected wherever we have

$$2\pi\,\sigma\chi + \phi = 2k\pi\ , \tag{2}$$

where k is an integer.

In the following we will assume that a grating spectrometer is used to disperse the fringes, as is the case with the GI2T, and that the fringes are imaged onto a detector whose coordinates are (x,y). The direction of dispersion is made parallel to the x axis, such that we have

$$\lambda = a\,x\ , \tag{3}$$

where a is proportional to the dispersion coefficient of the grating. We also assume that the direction of dispersion is perpendicular to the remapped pupil separation, so that the path-difference χ is only a function of y. We have therefore

$$\chi = \chi_o - b\,y\ , \tag{4}$$

where b depends on the pupil separation and the distance to the image plane, and χ_o is the optical path-difference at the center of the image. Equation (2) then becomes

$$2\pi\,\frac{\chi_0 - by}{ax} + \phi = 2k\pi\ , \tag{5}$$

which yields the equation of the fringes on the detector. The spectrum therefore contains a set

of diverging bright fringes whose paths are described by

$$(k - \phi/2\pi)\, ax + by - \chi_0 = 0 \quad . \tag{6}$$

The path difference due to the piston phase determines the origin $y_O = \chi_O / b$ of the fringes on the y axis, as well as their slope on the detector. As sketched on Figure 1, the slope of the fringes in the field indicates both the sign and magnitude of the path-difference χ_O. If we set b = 0 then equation (6) also describes a channeled spectrum.

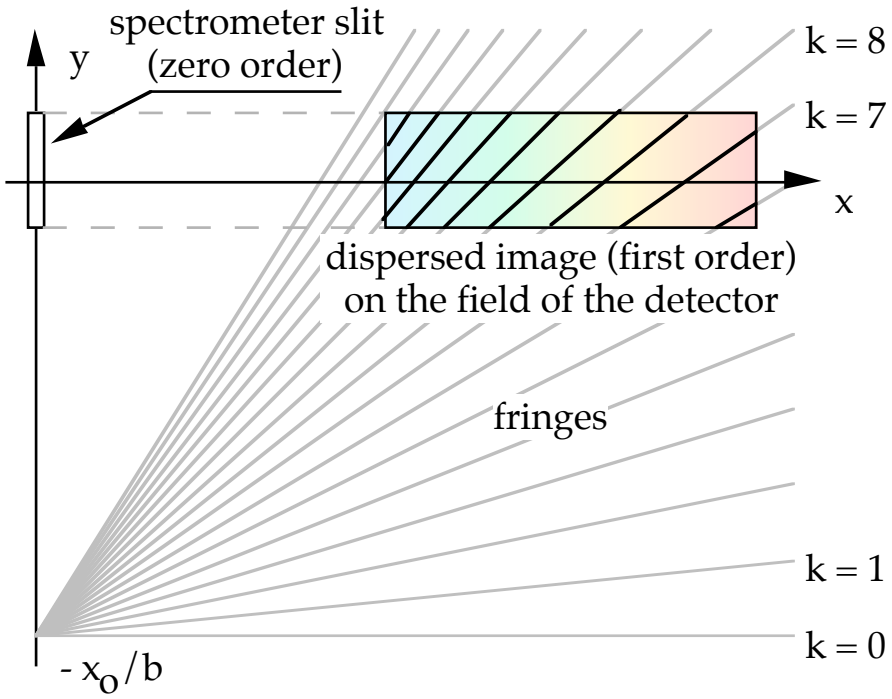

Figure 1. Dispersed fringes follow the equation of a set of diverging lines. The rectangular shaded area corresponds to the dispersed image field.

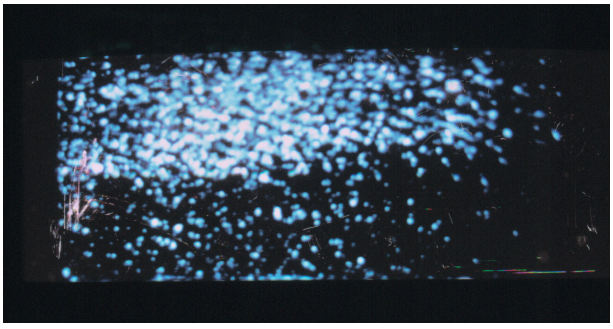

Figure 2. *Photograph of a dispersed image of a fringe pattern across a star.*

2. 2 Dispersed Fringes using Multi-r_0 apertures

With multi-r_0, apertures the effects of atmospheric turbulence across individual apertures cause the dispersed fringe pattern to be separated into numerous speckles as shown on Figure 2. Large scale phase variations further limit fringe measurements to a confined coherence volume, encompassing spatial, temporal, and chromatic phase changes.

Although each speckle contains a fringe pattern described in Eq. (1), fringes of different speckles have different phase relationships and therefore cannot be coherently combined. The average delay is derived from the integrated power spectra of individual fringed speckles, and the speckles must be processed individually in each frame. An image slicer is therefore used, whose slits' width corresponds to the speckle size; the detected spectrum shows the spectra of numerous speckles, but each is separated vertically at different locations in the image slice.

The number of speckles generated by atmospheric seeing is expressed as [3]:

$$N_s = \frac{1}{0.44}\left(\frac{D}{r_0}\right)^2, \tag{7}$$

where r_0 is Fried's coherence length and D the aperture diameter. For example, with D = 1.5 m and values of r_o in the order of 0.20 to 0.25 m, one gets $N_S \approx 100$. With the present optical setup at the GI2T, a single slice is used for the fringe tracker and approximately 12 dispersed speckles fit into the field of the detector. This corresponds to 10-15% of the light collected by the telescopes. The ways to improve this ratio are: a larger detector, or adaptive optics.

The atmospheric variations in phase evolve rapidly, and restrict the exposure time for individual frames of data. The coherence time of the atmosphere, τ_o, is typically between 1 and 10 ms in the visible, and the signal-to-noise ratio per exposure is maximized with exposures of near $2\tau_o$, allowing more photons to be gathered [4]. A fast algorithm, such as the one we describe in Sect. 3.2, is therefore necessary for real-time processing of the speckles in each exposure.

When two large apertures are used for fringe tracking, what is measured is the mean value of the delay between the two sampled wavefronts. The variation in piston phase across a large aperture has been derived previously by several authors [5 6 7]. If the spatial variations in phase are due to Kolmogorov turbulence, the phase structure function can be expressed as

$$D_\phi(r) = \left\langle \left| \phi(\rho + r) - \phi(\rho) \right|^2 \right\rangle = 6.88 \left(\frac{|r|}{r_0}\right)^{5/3}, \tag{8}$$

where r_0 is Fried's coherence length and r is an arbitrary separation between two points in the average wave plane. If the wavefront tilt is not compensated, the mean squared variations after piston phase is removed, measured over a diameter D, can be shown to be

$$\phi^2_{\rm rms} = 1.03 \left(\frac{D}{r_0}\right)^{\frac{5}{3}} . \qquad (9)$$

This is approximately true for the apertures of the GI2T, which is not presently equipped with adaptive optics, and whose star tracker corrects tilt up to 0.5 Hz. For the GI2T, the observed path variance is therefore twice as large as in eq. (9) and the rms spread is √2 times the above. The rms path difference is therefore

$$\Delta\chi_{\rm rms} = 0.229\,\lambda \left(\frac{D}{r_0}\right)^{\frac{5}{3}} . \qquad (10)$$

For an r_0 of 0.2 m and apertures of 1.5 m diameter, the rms variations in the visible are about 0.75 μm. The use of adaptive optics would reduce the numerical coefficient in eq. (9) (See table IV in reference 6.) For example, with the tilt completely removed the rms variations in path length become close to 0.25 μm. However, it would be difficult to stabilize a fringe pattern to better than $\lambda/4$, which requires the aberrations from the first ten Zernicke polynomials to be corrected. It follows that although it is possible for light from two large apertures to be combined coherently, the resolution in delay tracking is limited by the aperture size.

2. 3 Coherence Envelope and Tracking Resolution

To record the fringes at the GI2T, a spectrometer is used in conjunction with a 2D photon-counting array detector. The spatial information contained in the fringes is modified through the process of detection. Thus in the direction of dispersion the response is a convolution of the optical point spread functions of the spectrometer and detector. The power spectrum of this response determines the sensitivity to fringes as a function of path-difference. If the resolution is limited by sampling, the coherence length is determined by the bandwidth per pixel. If a bandwidth of $\Delta\sigma$ is dispersed across N spectral channels, then each channel represents a bandwidth of $\Delta\sigma/N$ and therefore a coherence length of $N/\Delta\sigma$, or approximately $N\lambda^2/\Delta\lambda$ Dispersing a large bandwidth in this way increases the coherence length by a factor of N. Losses may also occur due to sampling in the direction perpendicular to the dispersion, where the fringe spacing at red wavelengths may be larger than those at blue wavelengths. This spacing is determined by the remapped pupil separation and is a constant during the observations. It is therefore possible to choose a suitable separation and over-sample the red fringes, so that losses in the blue are rendered negligible.

Another consequence of the detection is that the spectrum is truncated, or windowed; the resolution in path-difference is limited by the Fourier transform of this window function [8] . The resolution is inversely proportional to the total detected bandwidth, and limited by the photon noise. By interpolation in the Fourier plane, the precision in the measurement of the path length difference χ can approach a fraction of a wavelength.

Fringe trackers may be broadly characterized by their ability to maintain the optical path difference equal to within a small fraction of the wavelength (λ), or within only a fraction of the coherence length ($\lambda^2/\Delta\lambda$). These modes are respectively referred to as cophasing and coherencing [9] . Cophasing keeps stabilized fringes visible at any exposure time. Coherencing lets phase fluctuations blur the fringes at long exposures.

Although in principle a system based on dispersed fringe tracking is capable of cophasing an interferometer, cophasing is only possible when the phase variations across each aperture are compensated to less than a fraction of a wavelength. For a multi-r_o aperture this would require some form of adaptive optics.

3 Principle of fringe tracking

3.1 Method of Delay Estimation

The optical delay in the center of the dispersed fringe image is sampled and used as an error signal for the fringe tracker control loop. Fringe slope and optical delay are related to one another by a linear relation, derived from equation (6) in the following.

On Figure 3. the optical delay χ_O is different from zero and fringes appear tilted. $\Delta\lambda$ and $\delta\lambda$ are respectively the total bandpass and the spectral fringe spacing. Δy and δy are respectively the vertical extent of the field and the vertical fringe spacings. The object phase ϕ is considered constant over the spectral bandpass and can therefore be omitted in the following.

For points (λ_1, y_1) and (λ_1, $y_1+\delta y$) on two adjacent fringes, relation (6) yields

$$k\lambda_1 + by_1 = \chi_O , \tag{11}$$

$$(k+1)\lambda_1 + b(y_1+\delta y) = \chi_O . \tag{12}$$

Subtracting the above expressions, the vertical fringe spacing δy can be expressed:

$$\delta y = \lambda_1 / b . \tag{13}$$

In the dispersion direction, for points (λ_1, y_1) and ($\lambda_1 - \delta\lambda$, y_1) on two neighboring fringes,

relation (6) becomes

$$k\lambda_1 + by_1 = \chi_o , \quad (14)$$

$$(k+1)(\lambda_1 - \delta\lambda) + by_1 = \chi_o , \quad (15)$$

Subtracting the above expressions yields

$$\delta\lambda = \lambda_1 / k . \quad (16)$$

At this point, fringe number k can be expressed as $k = (\chi_o - by_1) / \lambda_1$, we have therefore

$$\delta\lambda = \lambda_1^2 / (\chi_0 - by_1) , \quad (17)$$

The Fourier transform of such a quasi-periodic fringe pattern will show peaks at frequencies (U_p, V_p) and ($-U_p$, $-V_p$), such as on Figure 4. As the total field in the source image is $(\Delta x, \Delta y)$, and assuming a constant fringe spacing over the field, the relation between U_p and $\delta\lambda$ is the following:

$$U_p = \Delta x / \delta x = \Delta\lambda / \delta\lambda , \quad (18)$$

therefore, from equation (17)

$$U_p = (\chi_0 - by_1) \Delta\lambda / \lambda^2 . \quad (19)$$

The path length difference: $\chi = \chi_0 - by$, varies slightly with the vertical position in the image. The corresponding spread in the discretized Fourier space is negligible if:

$$\Delta\chi_{max} < \lambda^2 / \Delta\lambda , \quad (20)$$

where $\Delta\chi_{max}$ is the maximum path length variation across the image field. This is the case with the present GI2T recombiner. Equation (19) then becomes

$$\chi_0 . U_p \lambda^2 / \Delta\lambda . \quad (21)$$

This relation is used to derive the sign and amplitude of the optical delay in the interferometer. The relation does not depend on the sampling nor on any instrumental setting other than the wavelength and the total bandpass ($\Delta\lambda$) used.

The spatial frequency in the perpendicular direction is given by:

$$V_p = \Delta y / \delta y = b \Delta y / \lambda_1 . \quad (22)$$

V_p is not dependent upon the optical delay χ_o. However, U_p and V_p are wavelength dependent. In a broad band field, fringes are not equally spaced and parallel, and a two dimensional Fourier transform would not yield optimal results. One optical solution that has been thought of is a dispersed pupil: if the distance between remapped apertures in the pupil is made proportional to the wavelength, the fringe slope becomes wavelength independent. The solution presently implemented is numerical. The first step in a 2D Fourier transform would be the expression

$$\hat{I}(x . v_p) = \int I(x, y) \exp(-2i\pi y v_p) dy . \quad (23)$$

It is here replaced by

$$\hat{I}(x, v_p) = \int I(x, y) \exp\left(-2i\pi y \frac{v_p}{x}\right) dy \quad (24)$$

which has the same remapping effect as a dispersed pupil. Fringes need to be remapped in the other direction as well. The fringes are also distorted by barrel distortion caused by the image tubes in the detector. The images are therefore digitally remapped in real time prior to Fourier transform. The delay is then estimated from this modified two dimensional Fourier transform.

If the number of photons in a coherence volume leads to a sufficient signal to noise ratio, χ_0 can be sampled fast enough to allow coherencing. For fainter objects the signal to noise ratio in a single coherence volume becomes too low for fringe detection and χ_0 measurement: coherencing is no longer feasible. However, a time averaged χ_0 can be measured. Moduli of the Fourier transforms are averaged over a large number of frames until the peaks are high enough. This is possible because the phase effects of atmospheric seeing are zero average. In case of continuous drifts, as for example in a non stabilized space interferometer, there is another solution involving an xyt (3D) Fourier transform [10] [11].

3.2 Algorithm

For each frame, the computation must be completed in less than the coherence time, ($\tau_0 \approx$ 1 – 10 ms). Fortunately, only a small part of the Fourier plane needs to be searched, because the vertical fringe spacing is known a priori, and remains constant at each baseline.

The algorithm chosen for the 2-D Fourier transform takes advantage of the photon counting nature of raw images. Such images are usually sparse matrixes: a 100 K photons-per-second rate creates only 100 non-zero pixels in typical 1024 x 128, 1 ms frame. These images can be expressed as

$$I(x, y) = \sum_{i=1}^{n} \delta(x - x_i, y - y_i), \quad (25)$$

x_i and y_i are the coordinates of the i^{th} photon.

In the target Fourier plane only one frequency line per baseline needs to be computed. Let us consider a two-step approach to the 2-D Fourier transform. The first step is a 1-D transform along the y axis, for the single frequency V_p corresponding to the fringe spacing:

$$\hat{I}(x, v_p) = \sum_{i=1}^{n} \delta(x - x_i) \exp\left(-2i\pi y_i \frac{v_p}{x}\right) \quad (26)$$

This requires only one addition per photon, all trigonometric values being in tables. For n photons and B baselines, the number of computation steps is of the order of nB. It is much more efficient than an FFT over the whole frame. It is also more efficient than a sparse matrix

autocorrelation whose computation time is of the order of n^2.

Another advantage of this algorithm is the adjustment of V_p (in tables) to the local value of the fringe spacing in each spectral channel allowing precise computation over broad bandpasses.

The second step in the 2-D transform is a normal FFT along the x axis:

$$\hat{\mathbf{I}}(u, v_p) = \int \hat{I}(x, v_p) \exp(-2i\pi u x) dx . \quad (27)$$

This step has to be performed once every $2\tau_o$ and for every speckle in the multi-r_o aperture case.

4 Implementation

4.1 Optical layout

The standard GI2T recombiner is used. Its optical layout and image slicer have been described in reference 2 . It has not been modified for the moment as a single detector is used simultaneously for both for the ongoing astrophysical studies, and for the fringe tracker. A 40 nm bandpass is used, centered on the Hα line (656 nm) and 128 spectral channels. The spectral resolution is close to 0.4 nm and we get a fringe response suitable for detection over a path length difference of 500 μm. In the perpendicular direction a large over-sampling factor is used (18 pixels per fringe).

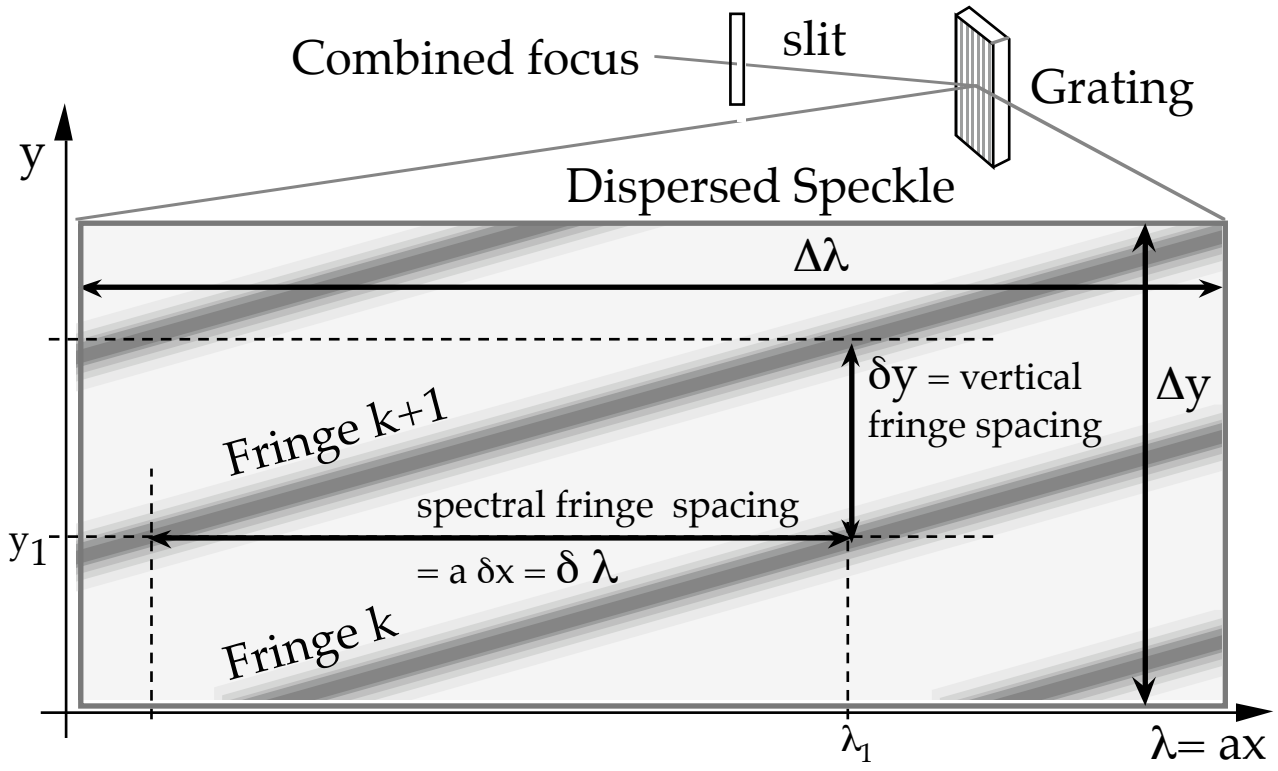

Figure 3. Fringes in a dispersed speckle in the image plane.

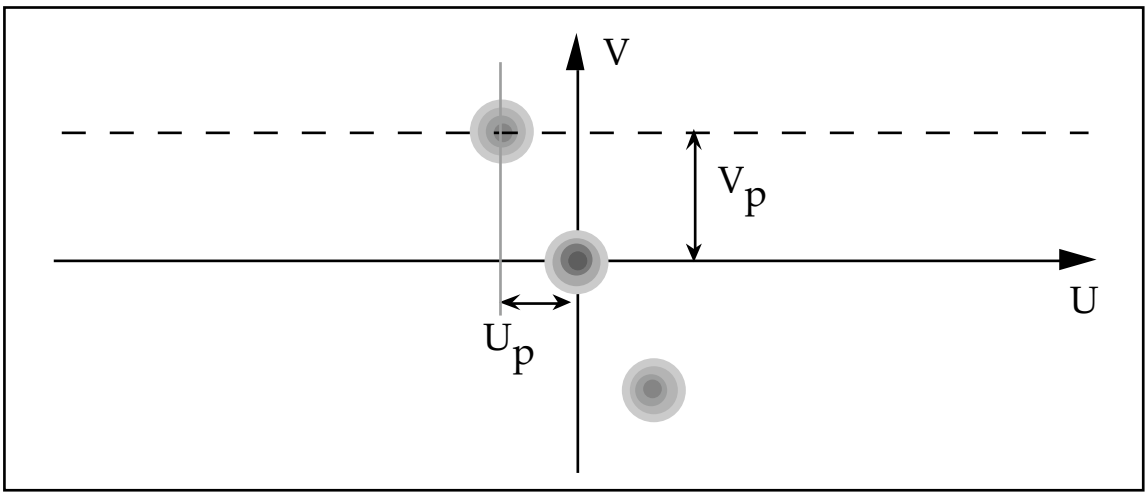

Figure 4. Peaks in the Fourier transform of the dispersed fringe image. The spatial frequency Up is related to the optical delay by the expression Up = co (Dl / l2) , where co is the optical path length at the center of the image.

4.2 Detectors and Data Acquisition

The dispersed image plane is sampled by a photon counting detector: the CP40 [12] . The CP40 is an intensified CCD camera with an extended-red S20 photocathode. An average of 250 x 600 pixels are used in the present setup. The detective quantum efficiency of this detector peaks at approximately 5.5%. It can operate to a maximum flux of 1200 photons per frame, limited by the camera digital electronics, and provides a fixed frame rate of 20 ms. A Ranicon detector [13] has also been used to allow the frame rate to be adjusted to the seeing conditions. This camera has been helpful in the implementation stage, but it is not used for fringe tracking, due to a limitation in photon flux ($1.5x10^4$ photons/s).

Once detected, photon coordinates are sent to computers: a RISC processor Macintosh for the real time optical delay computing and control, and HP workstations for data storage and off-line fringe visibility processing.

4.3 Control

The variance of the integrated modulus as a function of spatial frequency is sampled and compared to the peak value. When the signal reaches a given threshold, which may take from a few 20 ms frames to a few seconds, depending on the stellar visibility and magnitude, the

measured optical delay is used as an error signal for the delay line. It is interpolated in order to achieve a 1 μm resolution in path length difference. The delay line has been described in reference 2. The control loop is sketched on Figure 5. The fringe tracker can also be used in "scan mode". The coherencing length being on the order of 0.5 mm, fringes are usually found in a couple of steps.

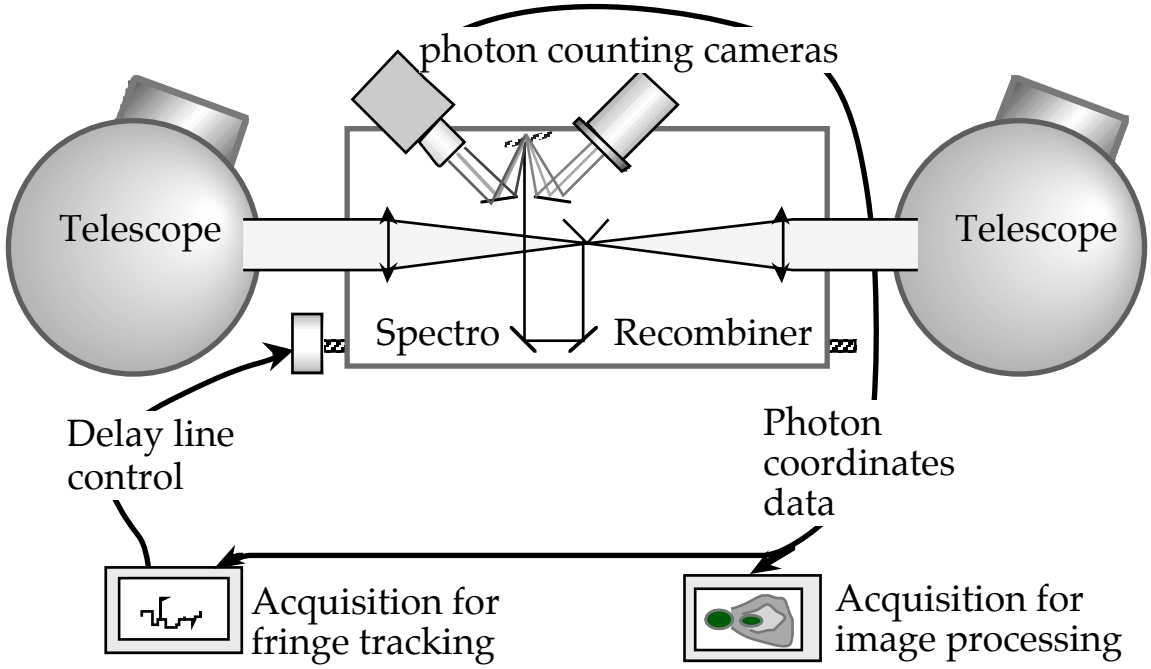

Figure 5. Fringe tracker control loop: single baseline setup for the GI2T.

5 Results

The stars β Lyr, γ Lyr, α Cep, δ Cep, and P Cyg were observed with the fringe tracker during the week of 1–6 August 1994. Figure 6 illustrates the performance of the fringe tracker during several of these runs. Each plot shows the results of about 30 minutes of observation, with the servo errors shown immediately above the observed changes in path-difference.

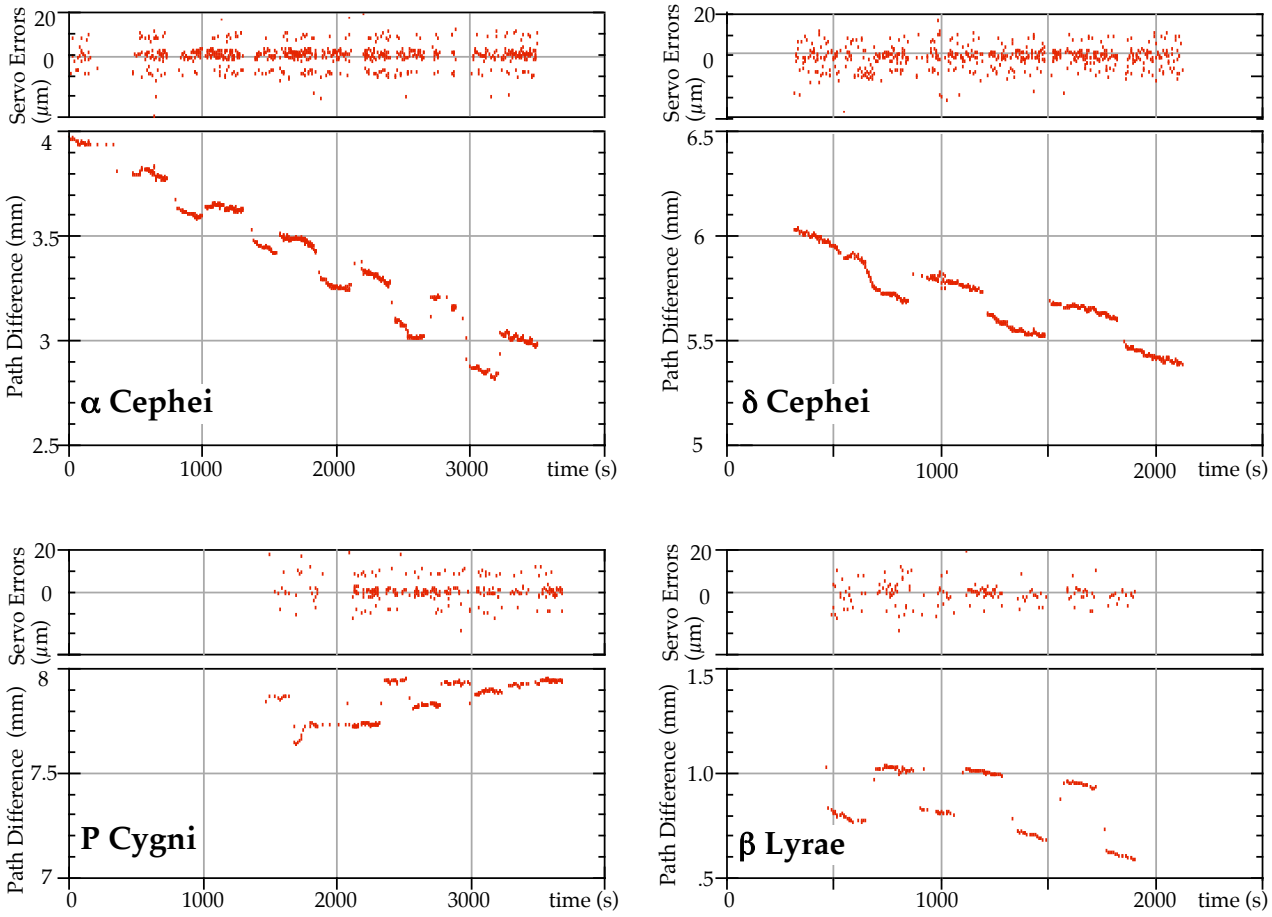

Figure 6 for manuscript # 10055: L.Koechlin et al. "Dispersed fringe tracking ...": Please print on two columns. Figure captions are at the end of the manuscript.

Figure 6. *Path-difference variations observed on four stars : α Cephei (with a 29 meters baseline), δ Cephei (29 meters), β Lyrae (51 meters), and P cygni (18 meters).The most noticeable feature in the path changes are the steps caused by the change in supports at the telescopes.*

The fringe tracker integrates the power spectra in real-time and calculates the signal-to-noise ratio of the integration. It resets the integration when either a threshold in signal-to-noise is reached, in which case a new delay estimate is assumed to be valid, or else the integration time exceeds a maximum time-out, and the information is discarded. During these observations, the fringe tracking system produced new estimates of the path errors every 2.9 – 9.6 seconds, and maintained the servo errors to 4.6 – 7.3 μm rms.

The features that are most readily discernible in each plot in Fig. 6 are caused by mechanical changes and errors in the baseline solution. In each plot there are discontinuities of ~ 200 μm about every 5 minutes. These are due to the spherical drives of the telescopes, which allow continuous tracking of a star for only a short duration. The drives of both telescopes are synchronized so that they reach their limit at the same time, and tracking is resumed after a break of ~ 40 seconds, during which time the drives are reset. Each plot also shows long term systematic drifts of up to 500 μm over 30 minutes, due to slight errors in the baseline solution. Atmospheric path variations are certainly present in each record, but account only for the fine structure that can be seen in each 5 minute segment.

The plot of P Cygni is the most remarkable in this series. It has a V magnitude of 4.8 and is the second faintest object for which fringes have ever been tracked with the GI2T – the faintest object being HR 7132 with a V magnitude of 5.6 (observed with a baseline of 16.3 m on June 7, 1995). During the observation in Fig. 7(d) the fringe tracker maintained the paths equal to 5.1 μm rms and produced estimates every 5.7 s on average, which is comparable to its performance with much brighter stars.

6 Remarks

Theoretical predictions suggested that if fringes could be observed using all the collected light on large telescopes [14] [15], a limiting magnitude would be reached between 13 and 17 with 1.5 m apertures. While 17^{th} magnitude has been reached by speckle interferometry on a 3.6 m telescope [16], no long baseline optical interferometer has ever observed objects much fainter than 5^{th} magnitude. The reason for this disparity is that interferometers must track fringes to maintain coherence between the apertures. The path-difference must be continuously measured and corrected.

The advantage of a multi-r_o aperture is that it allows a larger number of coherence areas to be sampled at the same time. For a large aperture, this in principle leads to an improvement proportional to the diameter D in the signal-to-noise ratio, but the field and processing power requirements increase with D^2. The slow development of an automated system for the GI2T has mainly been due to the lack of an adequate algorithm and sufficient computing power. The present recombiner samples approximately 12 speckles under the seeing conditions specified in section 2.2, and yields a gain of 3.5 in the signal-to-noise ratio over a comparable single-r_o system. At low light level conditions, the signal-to-noise ratio is proportional to the photon flux (see reference 15). Therefore in terms of limiting magnitude, this is a gain of 1.5 . The whole speckle pattern on a 1.5 m telescope, if analyzed, would yield a gain of 10 in the signal-to-noise ratio (2.5 magnitudes). Other parameters such as the optical throughput, the detector efficiency, and the angular extent of the observed objects, are responsible for the gap remaining between theoretical and observational limits.

As the aperture size increases, the transfer function of the instrument causes the fringe signal to spread out in the spatial frequency domain. The resulting loss has been noted by several authors [17] [18] . This problem is overcome by integrating – around – , the peak of the fringe signal, rather than sampling the peak height [19] and that is done automatically by the fringe tracker.

7 Conclusion

The new fringe tracker of the GI2T currently provides correction for path-variations with an accuracy of ≈ 5 μm rms. It takes advantage of the interferometer's large apertures and relatively broad spectral bandpass (40 nm) without constraining the coherence length. It has benefited the instrument by providing rapid fringe acquisition, and, as demonstrated by the observations of P Cygni and HR 7132, an extended limiting magnitude.

We have shown that despite the lack of adaptive optics in the GI2T, it is yet possible to take advantage of multi-r_o apertures to track fringes in dispersed stellar spectra. This method has the potential of enhancing the performance of future large telescopes arrays, either multi-speckle, or diffraction limited. It has already allowed the GI2T to track on objects that, to the authors' knowledge, are fainter than those observed by any other stellar interferometer.

Acknowledgments

The authors are grateful for the help of Antoine Labeyrie, Luc Arnold, Guy Merlin, and Jean Pinel. They are also thankful to Francesco Paresce, Knute Ray, and Colin Cox for their help with the Ranicon detector. LK acknowledges the support of funding from the the Programme National de Haute Résolution Angulaire en Astrophysique and the Groupe De Recherches Milieux circum-stellaires. PRL was funded in this study by the Centre National de Recherche Scientifique and the Conseil Général des Alpes Maritimes through an Henri Poincaré Fellowship at the Observatoire de la Cote d'Azur. The GI2T is maintained and operated with the support of the Programme National de Haute Résolution Angulaire en Astrophysique.

When this work was performed P.R. Lawson was with the Observatoire de la Cote D'Azur. He is now with the Mullard Radio Astronomy Observatory, Cavendish Laboratory, Madingley Road, Cambridge CB3 0HE, UK.

References

[1] A. Labeyrie, G. Schumacher, M. Dugué, C. Thom, F. Foy, D. Bonneau, and R. Foy, "Fringes obtained with the large boule interferometer at CERGA," Astron. Astrophys. **162,** 359-364 (1986).

[2] D. Mourard, I. Tallon-Bosc, A. Blazit, D. Bonneau, G. Merlin, F. Morand, F. Vakili, and A. Labeyrie, "The GI2T interferometer on Plateau de Calern," Astron. Astrophys. **283,** 705-713 (1994).

[3] C.Aime, "Measurement of averaged squared modulus of atmospheric-lens modulation transfer function"J. Opt. Soc. Am. **64**, 1129-1132 (1974)

[4] F. Roddier, "Atmospheric limitations to high angular resolution imaging," in ESO Conference Proc. on "Scientific Importance of High Angular Resolution at Infrared and Optical Wavelengths," (ESO: Garching, 1981) pp. 5-23.

[5] D.L. Fried, "Statistics of a geometric representation of wavefront distortion," J. Opt. Soc. Am. **55,** 1427-1434 (1965).

[6] R.J. Noll, "Zernike polynomials and atmospheric turbulence," J. Opt. Soc. Am. **66,** 207-211 (1976).

[7] R.A. Sasiela, Electromagnetic Wave Propagation in Turbulence, (Springer - Verlag: Berlin, 1994), pp. 63-65.

[8] P. R. Lawson, "Group delay tracking in optical stellar interferometry using the Fast Fourier Transform," J. Opt. Soc. Am. A. **12** , 366-374 (1995).

[9] J.M. Beckers, "Cophasing telescope arrays," in *Difffraction-Limited Imaging with Very Large Telescopes* , D.M. Alloin and J.M. Mariotti eds., (Kluwer: Dordrecht 1989) pp. 355-34.

[10] L. Koechlin, "The I2T interferometer," in High Resolution Imaging by Interferometry, J. M.

Beckers ed., (European Southern Observatory, Garching bei München, 1988) pp. 695-704.

[11] L. Koechlin, "Active fringe tracking," in – High Resolution Imaging by Interferometry II, – J.M. Beckers and F. Merkle, ed. (European Southern Observatory, Garching bei München, 1992) pp. 1239--1246.

[12] A. Blazit "A 40mm photon counting camera" in proceedings of "Image Detection and Quality", Proc. Soc. Photo-Opt. Instrum. Eng. p. 259-263 (1986).

[13] M. Clampin, J. Crocker, F. Paresce, M. Rafal "Optical Ranicon detectors for photon counting imaging. I." Review of Scientific Instruments, **59**, 8, p. 1269-1285 (1988).

[14] A. Labeyrie, "Stellar interferometry methods," Ann. Rev. Astron. Astrophys. **16,** 77-102 (1978).

[15] F.Roddier and P.Léna " Long baseline Michelson interferometry with large ground-based telescopes operating et optical wavelengths" J.Optics (Paris) **15**, 4, p. 171-182 (1984)

[16] R. Foy, D. Bonneau, A. Blazit, "The multiple QSO PG1115 +08: A fifth component." Astron. Astrophys. **149,** L13-L16 (1985).

[17] W. J. Tango and R. Q. Twiss, "Michelson stellar interferometry," Prog. Opt. **17**, 239-277 (1980).

[18] D. Buscher, "Optimizing a ground-based optical interferometer for sensitivity at low light levels," Mon. Not. R. Astr. Soc. **235**, 1203-1226 (1988).

[19] D. Mourard, I. Tallon-Bosc, F. Rigal, F. Vakili, D. Bonneau, F. Morand, and Ph. Stee, "Estimation of visibility amplitude by optical long-baseline Michelson stellar interferometry with large apertures", Astron. Astrophys. **288**, 675--682 (1994).